Chapter 9.
Multifractals and dynamical systems.
September_22_2016.

9.1. Introduction.

In Chapter 8 we saw that chemical reactions in open flow chemical reactors are intrinsically unstable and highly sensitive to flow rates, temperature gradients, heat loss from the reactor and competition for supply of nutrients and heat from simultaneous reactions. The analogue is with a camp fire that can simply smoulder for want of oxygen or ignite and operate as a highly correlated bonfire with high efficiency in fuel consumption. The smouldering campfire is the equivalent of a low grade, disseminated mineral deposit; the roaring camp-fire is the equivalent of a high grade mineral deposit with strongly correlated spatial distributions of alteration and mineralisation. The transition from smouldering camp-fire to roaring camp-fire is a critical transition and we need to understand if the transition from a disseminated to high grade deposit is also a critical transition.

The chemical engineer can monitor the operation of a chemical reactor and see if the reactor is approaching or has passed the critical stage. We do not have the luxury of monitoring a mineralising system in real time and so we need some tools that enable us to measure if a mineralising system is sub-critical, critical or super-critical. One way of doing this we suggest arises from the metrics of the multifractal singularity spectrum. We discuss here the features of the singularity spectrum that are characteristic of systems as they pass from sub-critical to super-critical and show that these same characteristics arise in mineralised systems. In essence, the transition through criticality is marked by a sudden broadening of the singularity spectrum. In this Chapter we show that its broadening delineates low grade deposits from high grade deposits and In Chapter 11 we elaborate on this observation for gold deposits of the Yilgarn in Western Australia.

The questions we want to answer in this chapter are:

What is a wavelet transform and how is it related to multifractal geometry? *How does one characterise and measure long range correlations*? *Does the multifractal character differ from small, low grade mineral deposits to large, well mineralised systems*? *Are there features of the multifractal spectrum that correlate with sub-critical, critical and super-critical systems*? *Is there any relation between the multifractal spectrum and classical spatial statistics used in developing grade models*?

9.2. The wavelet transforms.

Although box counting procedures can be used to explore multifractal geometries, the process is quite cumbersome and can produce erroneous results especially if the singularity measure varies significantly within box sizes greater than a given value (see Arneodo et al., 1987, 1995). We require a fast, compact and quantitative characterisation of seemingly complex data sets that is readily applicable to 1, 2 and 3 dimensional situations and so we turn to a *wavelet* based system. The wavelet approach has many advantages over box counting procedures although a wavelet is basically a "generalised box". Methods of multifractal analysis based on the wavelet transform are particularly applicable to self-similar, intermittent data sets where the wavelet acts as a "microscope" that can zoom into the details of the signal and define local structure and singularities. Wavelet based software now exists that makes fractal and multifractal analysis fast and efficient so that complex data sets can be completely analysed within minutes using a laptop computer. In addition the wavelet approach is reasonably well established within a thermodynamic framework (Bohr and Tel,

1988; Arneodo et al., 1995) so that the procedures and results can be placed within a broader mechanics framework.

First let us explore the multifractal concept in greater detail. As we have indicated a multifractal consists of groups of fractal objects interwoven in space. The resulting geometry may or may not appear self-similar depending on the complexity of the inter-relations between the various fractals. It is common (Fedor, 1988) to represent the range of singularity measures for multifractals by the expression

$$N_\alpha(\varepsilon) = \varepsilon^{-f(\alpha)} \qquad (9.1)$$

which is a generalisation of (6.1) so that D in (6.1) is replaced by a spectrum, $f(\alpha)$, of singularity measures. α is commonly known as the *Holder exponent* and is also known as the Lipshitz exponent. The function $f(\alpha)$ appears as a $\cap$ – shaped curve represented by a plot of $f(\alpha)$ against α as shown in figure 6.5 (c). As complex geometries continue to be explored other representations and methods of analysis of multifractals appear (Arneodo et al., 1995; Venugopal et al., 2006) with extensions to two and three dimensions (Arneodo et al., 2003). The future development of these procedures represents an enormous opportunity to explore and quantify the geometry of fabrics in metasomatic rocks and so add to our knowledge of complexity, and the associated mechanisms, in metasomatic fabrics and processes.

9.2.1 Wavelet analysis. What is a wavelet?

We introduced the concept of *wavelets* in Chapter 6. A *wavelet* can be thought of as a *generalised box*. In fact some wavelets (for instance, the Haar wavelet, figure 9.1a) have a box-like shape. For the most part a wavelet has a localised wave-like shape and is designed to emphasise particular aspects of the signal to be analysed. Libraries of wavelets can be found in *Mathematica*® and some examples are shown in figure 9.1.

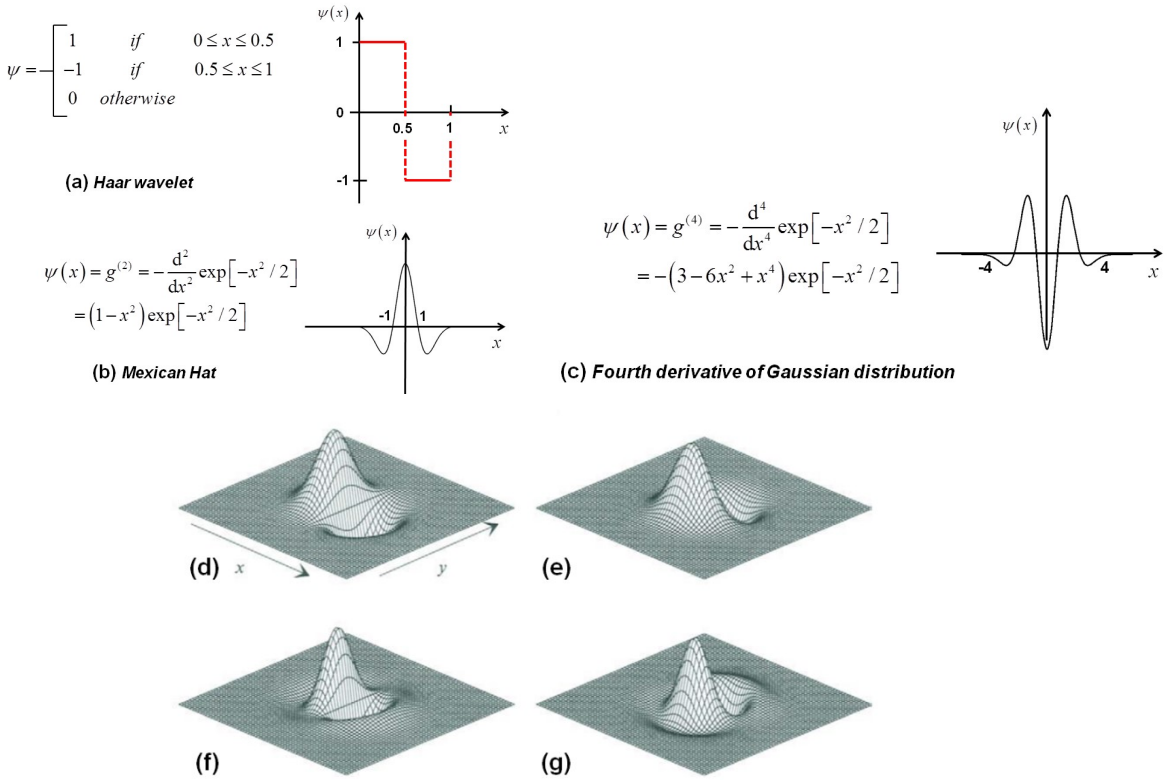

Figure 9.1. Examples of one- and two- dimensional wavelets. (a) to (c) One-dimensional wavelets. (a) The Haar wavelet. (b) The Mexican hat wavelet; this is $g^{(2)}$. (c) The fourth derivative of a Gaussian distribution: $g^{(4)}$. (d) to (g) Two-dimensional wavelets after Arneodo et al. (2003) . (d), (e) First order derivatives with respect to x and y for a Gaussian function. (f), (g) First order derivatives with respect to x and y for a Mexican hat function.

The wavelet transform (WT) of a signal, $\hat{s}$, consists of decomposing $\hat{s}$ into space-scale contributions that are defined by the *analysing wavelet*, ψ which is chosen to be localised in space and commonly of zero mean although $g^{(0)}$ (see (9.2)) is sometimes used where $g^{(0)}$ is the Gaussian function (Arneodo et al, 1995). A class of commonly used wavelets is defined by the successive derivatives of the Gaussian function:

$$\psi(x) = g^{(N_\psi)}(x) = (-1)^{N_\psi+1} \frac{\mathrm{d}^{N_\psi}}{\mathrm{d}x^{N_\psi}}\left[\exp\left(-x^2/2\right)\right] \qquad (9.2)$$

$g^{(2)}$ and $g^{(4)}$ are shown in Figures 9.1 (b, c). N_ψ is the order of the differentiation involved in the formation of the wavelet. Note that various conventions are adopted in the literature with respect to the form of (9.2) and in some instances the $(-1)^{N\psi+1}$ term is omitted. The WT of the function $\hat{s}$ is defined as the convolution of $\bar{\psi}$ with $\hat{s}$:

$$W_\psi[\hat{s}](b,a) = \frac{1}{a}\int_{-\infty}^{+\infty} \bar{\psi}\left(\frac{x-b}{a}\right)\hat{s}(x)\,\mathrm{d}x \qquad (9.3)$$

where b is the space parameter, $a > 0$ is the scale parameter and $\bar{\psi}$ is the complex conjugate of ψ. The quantity $W_\psi[\hat{s}](b,a)$ is known as the *wavelet coefficient* at the scale a and around the point $x = b$. The procedure involved in a wavelet analysis is to select a *mother wavelet*, ψ, and contract or extend ψ by successive scales a. For each scale the wavelet is scanned across the image with the same procedure as for box counting so that $W_\psi[\hat{s}](b,a)$ is evaluated at each point, b, and for each scale a. The local behaviour of $\hat{s}$ is reflected in the wavelet transform which behaves as

$$W_\psi[\hat{s}](x_0,a) \sim a^{\alpha(x_0)} \qquad (9.4)$$

where x_0 is a selected point and α is the *Holder exponent*. Some examples of wavelet transforms are given in figures 9.2 and 9.3. The wavelet transform contains all the information needed to establish the fractal geometry of an object (Arneodo et al., 1995).

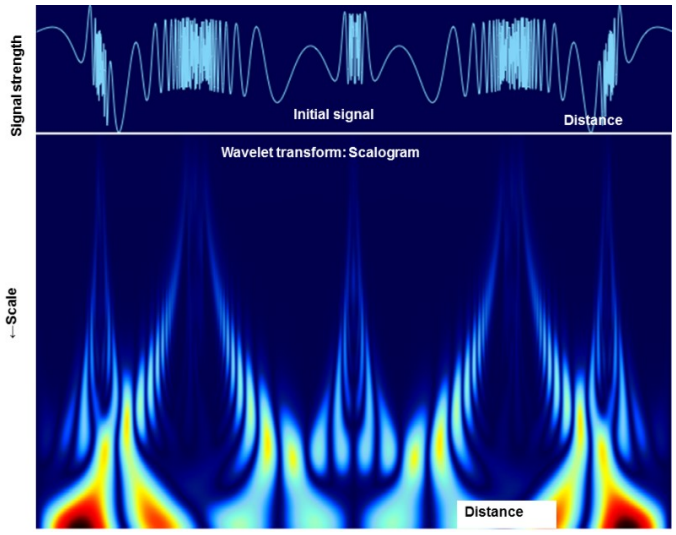

Figure 9.2. An example of an observed signal (top) and the resulting wavelet transform (lower). The changes in frequency in the signal are easily observed in the transform.

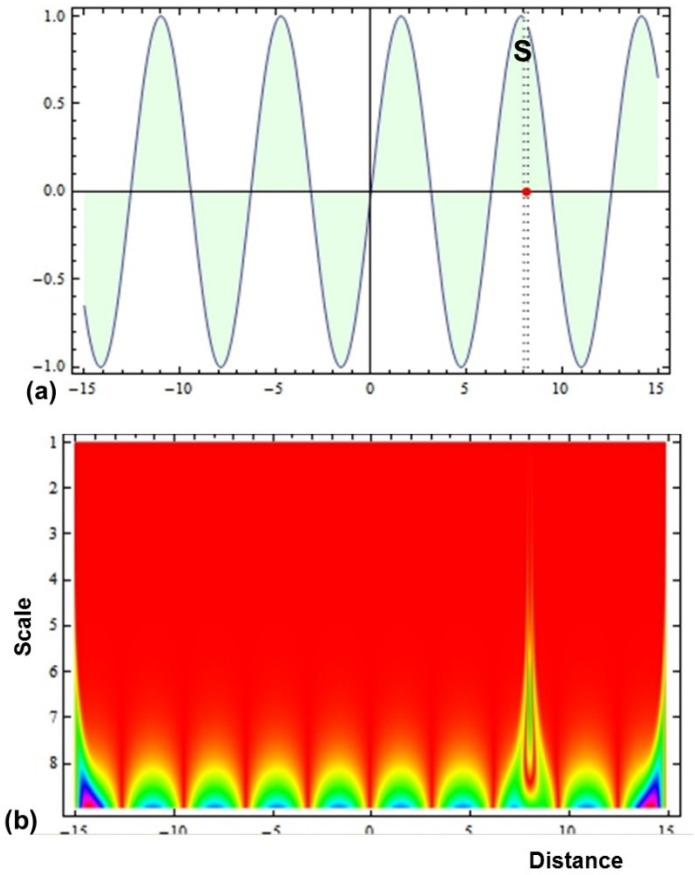

Figure 9.3. Another example of an observed signal (a) with resulting wavelet transform (b). Notice that the very small discontinuity in the signal at S is easily detected in the transform.

9.2.3. How do you establish the singularity strength, α?

In Figure 9.4 (a) a signal is shown comprising a singularity, S, and a gaussian "hump", G. This example serves not only how to establish the singularity measure, α, for the singularity, S, but also gives some insight into the wavelet transform method of analysing signals. In Figure 9.4 (b) the *scalogram* for the signal in Figure 9.4 (a) is given. The analysing wavelet is $g^{(1)}$ **.** The scalogram consists of the intensity of the wavelet transform, W_ψ, contoured on a plot of the wavelet scale, a, against the distance along the signal, x. The singularity is centred at $x = -512$ whilst the Gaussian hump is centred at $x = +512$.

Three dimensional renditions of the scalogram are given in Figure 9.4 (c, d) showing a strong minimum corresponding to the singularity with a maximum either side of the minimum; the two maxima coallesce at the singularity (Figure 9.4 d). The Gaussian hump is represented by two maxima either side of the peak of the hump. This diagram is an example of a general feature of scalograms, namely, that there is always at least one maximum in W_ψ that points at the singularity. The actaul number of maxima lines that point to the singuality is $(N_\psi + 1)$ where N_ψ is the order of the mother wavelet. No maxima lines point to the Gaussian hump which is not a singularity.

The value of the singularity strength, a, is given by the slope of the red line marked A-B in Figure 9.4 (d) plotted in log-log space (Figure 9.4 f). This example is discussed in detail by Arneodo et al. (2002).

9.2.4. The WTMM method.

The wavelet method we elect to use is the *Wavelet Transform Maximum Modulus (WTMM)* method developed by Bacry et al. (20xx). The *WTMM* method (Mallat and Hwang, 1992) consists of evaluating the *partition function*:

$$\mathbb{Z}(q,a) = \int \left| W_\psi [\hat{s}](x,a) \right|^q \mathrm{d}x \qquad (9.5)$$

at each point on the signal $\hat{s}$. The meaning of the integral in (9.5) is as follows. We consider a section across a scalogram at a specific value of the scale, *a*, as shown in Figure 9.5 (a). This represents the value of $W_\psi [\hat{s}](x,a)$ for the value of *a* selected. The absolute value of this signal, $\left| W_\psi [\hat{s}](x,a) \right|$, is shown in Figure 9.5 (b). This corresponds to $q = 1$. In subsequent figures (Figures 9.5 c, d) we show the second and third moments, $\left| W_\psi [\hat{s}](x,a) \right|^2$ and $\left| W_\psi [\hat{s}](x,a) \right|^3$ corresponding respectively to $q = 2$ and $q = 3$. Similar moments can be constructed for other values of *q*. As an example, the value of the integral for $q = 2$,

$$\mathbb{Z}(2,a) = \int \left| W_\psi [\hat{s}](x,a) \right|^2 \mathrm{d}x$$

is the area under the curve in Figure 9.5 (c) with similar statements for all other values of *q*.

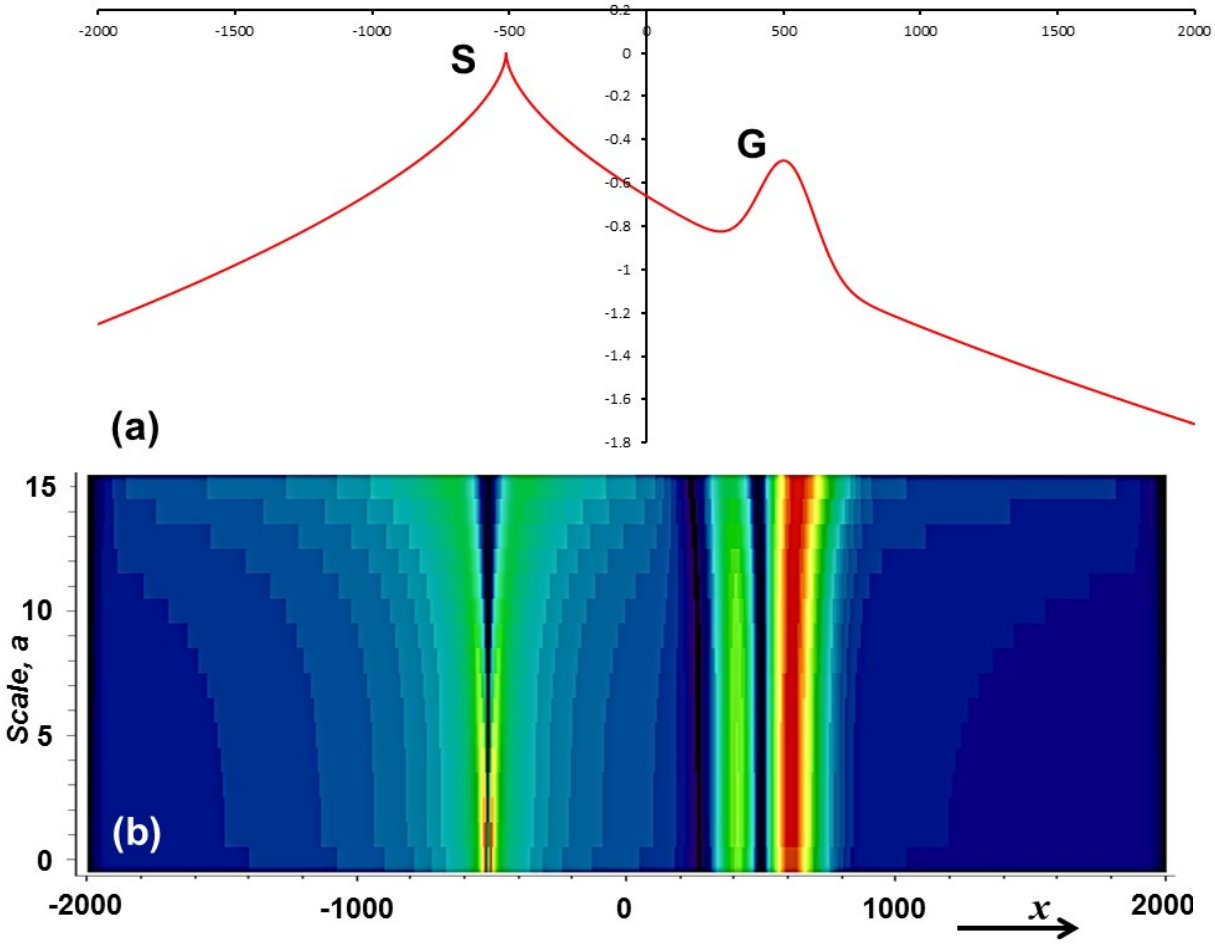

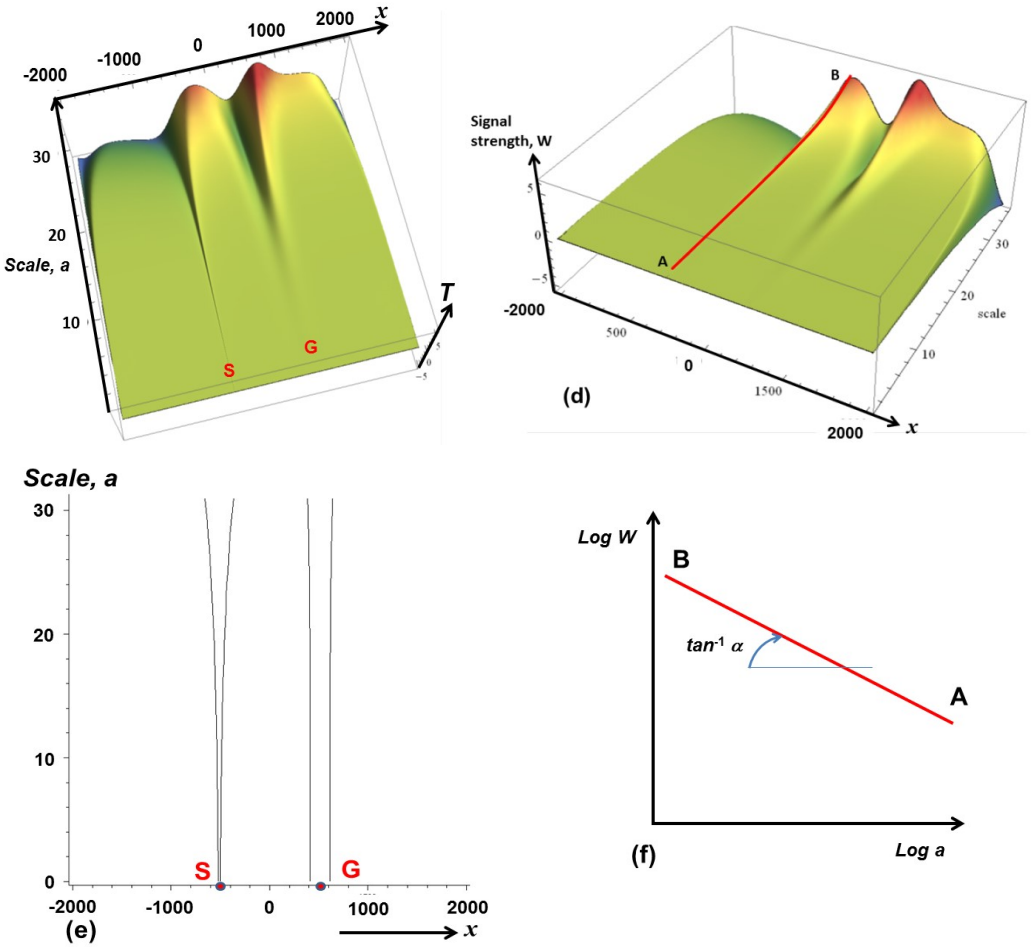

Figure 9.4. The procedure involved in establishing α and $f(\alpha)$. (a) A signal given by $f(x) = -\left|\frac{x-x_0}{1024}\right|^{0.6} + \frac{1}{2}\exp\left(-\frac{1}{2}\left(\frac{x-x_1}{100}\right)^2\right)$ which shows a singularity, S, at x_0 = -512 and smooth non-singular behaviour at x_1 = +512 corresponding to G. (b) The wavelet transform of (a). (c) Three dimensional version of (b) showing the positions of S and G. (d) Three dimensional version of (b) highlighting the slope of the wavelet transform along A-B towards S. (e) Scalogram showing the maxima in (b). The maxima lines converge on the singularity, S, but not on the non-singulatity, G. (f) Definition of the singularity strength, α, as the slope of the plot of log W_ψ against log a.

We are now in the position to plot a value of $\mathbb{Z}(q,a)$ at a given value of a for all chosen values of q as shown in Figure 9.6 (a).

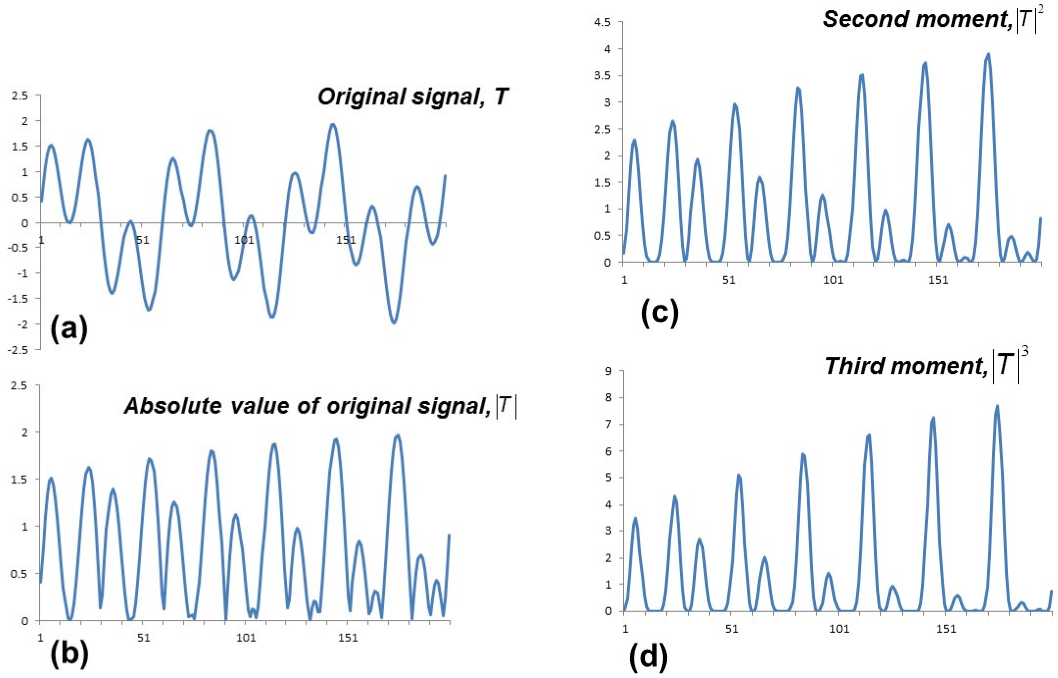

Figure 9.5. Examples of the moments of the signal, T, given in (a). (b) The first moment of T. (c) The second moment of T. (d) The third moment of T.

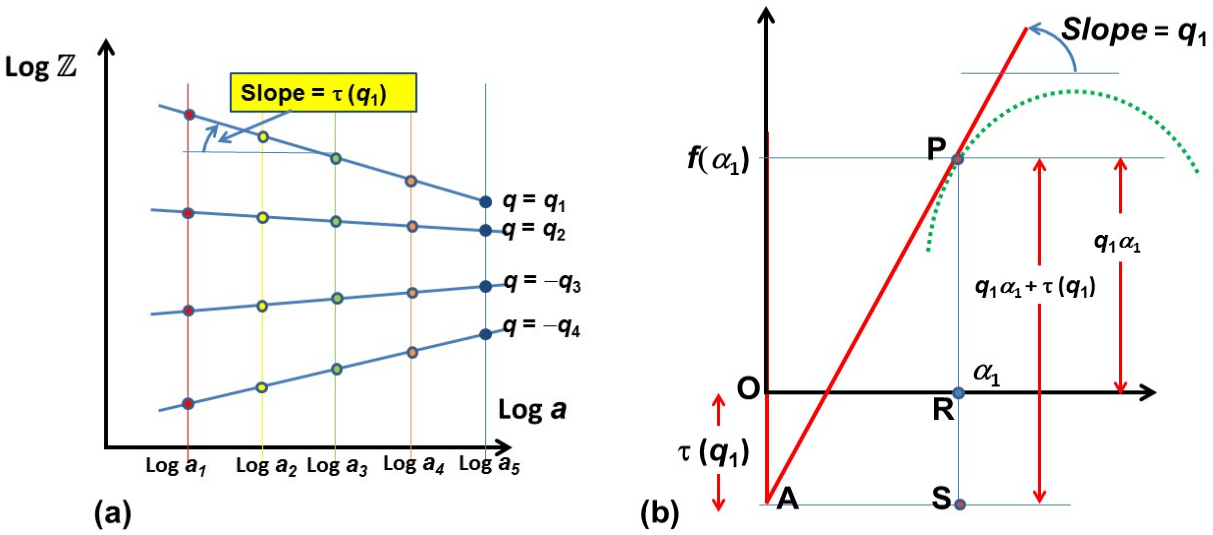

Figure 9.6. The constructions needed to produce the $f(\alpha)$ spectrum. (a) For a selected value of a (say a_1) The value of $\mathbb{Z}(q, a_1)$ is plotted (as red dots) on a log $\mathbb{Z}$ – log a diagram. The $\mathbb{Z}(q, a_1)$ are obtained as the areas under the curves in Figure 9.5. This is repeated for new values of a in order to obtain the columns of yellow, green, orange and blue dots. If the signal is multifractal all dots for a given q lie on a straight line. The slope of each line is $\tau(q)$ as in (9.7). (b) For a given α (say α_1, obtained from Figure 9.4 (f) we draw a line normal to the α-axis. $\tau(q_1)$ is marked as OA. A line with slope q_1 is drawn as AP. The distance PS is now equal to $[q_1\alpha_1 - \tau(q_1)]$ which is the Legendre transform of $\tau(q_1)$. Another way of thinking about this is that the equation of the line AP and similar lines with slope , q, is $f(\alpha) = [q\alpha - \tau(q)]$ The distance PR is equal to $f(\alpha_1)$. If this is repeated for all the q and $\tau(q)$ then the singularity spectrum is traced out as indicated by the green dotted curve.

The procedure outlined above is straightforward for $q \geq 0$ but fails for $q < 0$ whenever $W_\psi[\hat{s}](x_0, a) = 0$ since $\mathbb{Z}$ becomes infinite. For this reason, $\mathbb{Z}(q, a)$ is evaluated for each value of a by noting the *maximum* in $W_\psi[\hat{s}](x_0, a)$ for all scales a' where $a' \leq a$ as

shown in Figure 9.7. This maximum is denoted by $\sup_{(x,a')}\left|W_\psi[\hat{s}](x,a')\right|$. Thus (9.5) is replaced by:

$$\mathbb{Z}(q,a)=\sum_l\left(\sup_{(x,a')}\left|W_\psi[\hat{s}](x,a')\right|^q\right) \tag{9.6}$$

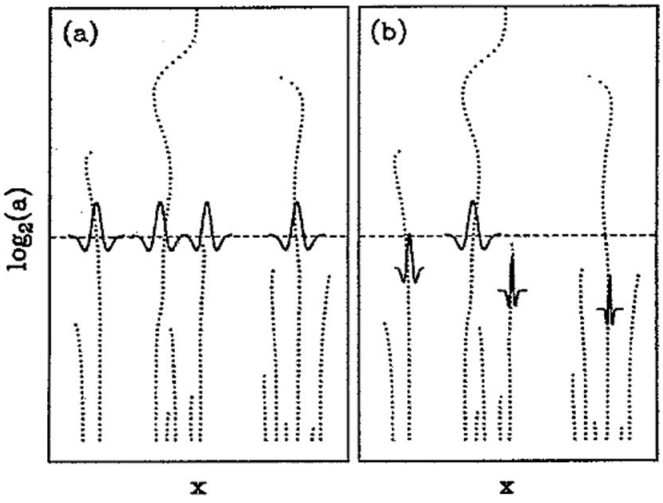

Figure 9.7. The significance of the maximum value of $W_\psi[\hat{s}](x_0,a)$. (a) Plot of the logarithm of the scale against *x*. The wavelet is scanned across the signal at a given value of the scale. (b) The wavelet is scanned but only the maximum for a given value of $W_\psi[\hat{s}](x_0,a)$ is selected. This maximum is $\sup_{(x,a')}\left|W_\psi[\hat{s}](x,a')\right|$

This procedure allows one to establish the exponents $\tau(q)$ as

$$\mathbb{Z}(q,a)\sim a^{\tau(q)} \tag{9.7}$$

Then by taking the Legendre transform of $\tau(q)$ we obtain:

$$f(\alpha)=\min_q\left(q\alpha-\tau(q)\right) \tag{9.8}$$

This is best done (Arneodo et al., 1995) by first calculating

$$\hat{W}_\psi[\hat{s}](q,l,a)=\frac{\left|\sup_{x,a'}W_\psi[\hat{s}](x,a')\right|^q}{\mathbb{Z}(q,a)} \tag{9.9}$$

Then $\alpha(q, a)$ follows as

$$\alpha(q,a)=\sum_l\ln\left|\sup_{x,a'}W_\psi[\hat{s}](x,a')\right|\hat{W}_\psi[\hat{s}](q,l,a) \tag{9.10}$$

and

$$f(q,a)=\sum_l\hat{W}_\psi[\hat{s}](q,l,a)\ln\left[\hat{W}_\psi[\hat{s}](q,l,a)\right] \tag{9.11}$$

These calculations can be performed in a relatively painless and efficient manner using software such as *LastWave* (Arneodo, A., Audit, B., Kestener, P. and Roux, S. 2008. Wavelet-based multifractal analysis. Scholarpedia 3, 4103. doi:10.4249/scholarpedia.4103. **Error! Hyperlink reference not valid.**http://www.cmap.polytechnique.fr/~bacry/). Alternative software is *WaveLab* (Buckheti, J., Chen, S., Donoho, D., Johnstone, I., Scargle, J. About WaveLab. Version .850 December, 2005. http://www-stat.stanford.edu/~wavelab/). The method has been extended to two dimensions by Arneodo et al. (2000), Decoster et al. (2000) and Arneodo et al. (2003) and to three dimensions by Kestener and Arneodo (2003, 2004, 2007) and Arneodo et al. (2003). Some comparisons between different methods for analysing singularity spectra and results are given by Turiel et al. (2006).

We give an example below of the WTMM method applied to a non-uniform Cantor set (figure 9.9 a). The example is taken from a demonstration included in the *LastWave* software. We also show the uniform triadic Cantor set in figure 9.9 (b). This is formed by uniformly removing the central one third of the signal and then repeating the procedure as shown in the figure. The WTMM method is applied to this fractal by Arneodo et al. (1995, §3.3.2, figure 3) and the result is that for a monofractal with a fractal dimension of (ln2/ln3). The production of monofractals such as this requires an ordered and coordinated process whereby each level of subdivision follows a precisely defined law. It is amazing that some DNA sequences are monofractals (Arneodo et al., 1995). For the most part in natural examples such order is not followed and multifractals develop. An example is the generalised non-uniform Cantor set shown in figure 9.9 (a). The maxima lines from the wavelet transform of the signal are shown in figure 9.9 (b). Plots of $\mathcal{Z}(q, a)$ against $\log_2 a$ are shown in figure 9.9 (c) from which the $\tau(q)$ spectrum may be derived in figure 9.9 (d). The observation that the $\tau(q)$ versus q curve is nonlinear is the hallmark of a mutifractal distribution; for the uniform Cantor set such a curve is linear. Finally the $f(\alpha)$ spectrum is given in figure 9.9 (e) showing a well defined multifractal spectrum with a support given by $f(\alpha) \approx 0.8$ at $\alpha \approx 0.75$.

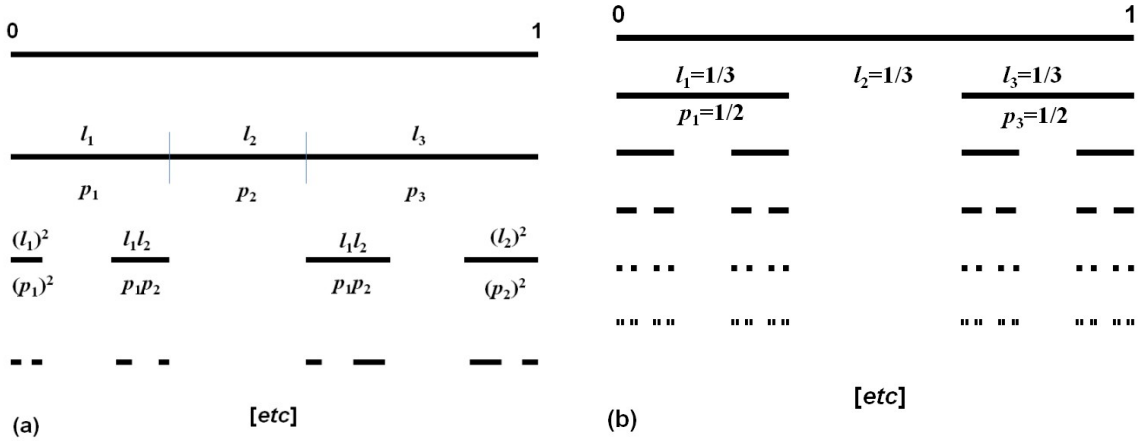

Figure 9.8. Cantor sets. (a) A generalised Cantor set divided initially into lengths, l_1, l_2 and l_3.with an initial probability of selection of p_1, p_2 and p_3. (b) A uniform Cantor set where $l_1 = l_2 = l_3$ and $p_1 = p_2 = p_3$.

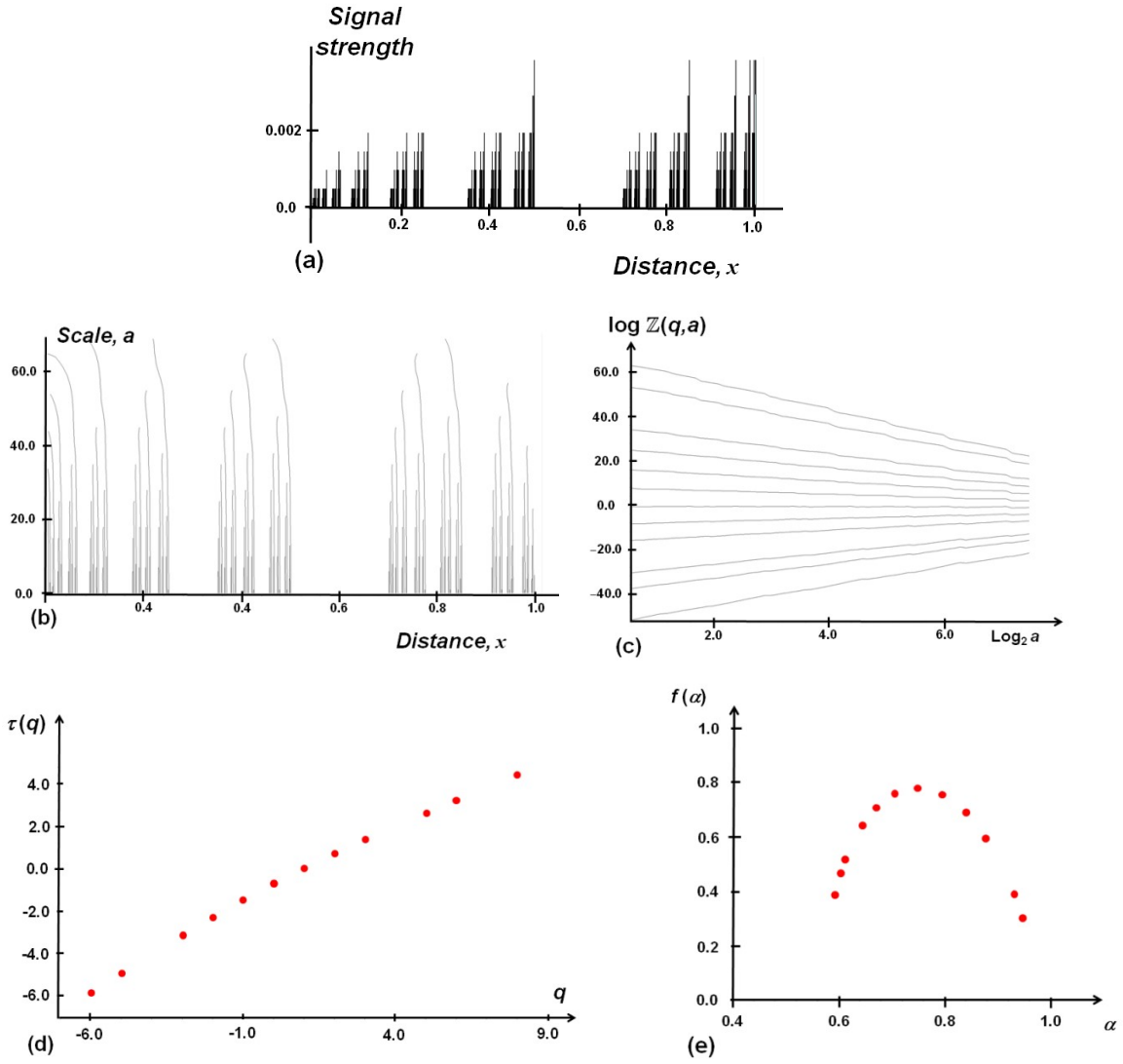

Figure 9.9. WTMM analysis of non-uniform Cantor set. (a) The signal to be analysed. (b) Map of the maxima lines from the wavelet scalogram. (c) The $\mathbb{Z}(q, a)$ spectrum. (d) The $\tau(q)$ spectrum. (e) The $f(\alpha)$ spectrum.

9.3. The work flow involved in a wavelet analysis.

The work flow involved in analysing a given data set is summarised below.

- The initial data set (Figure 9.10 a) is expressed in digital format. In some instances it may be useful to process the data in some manner to remove overall trends and high frequency noise or to standardise the data interval. Details of these procedures are given in Sprott (2003).
- The wavelet transform is prepared as shown as a scalogram in Figure 9.10 (b). This can be done using various software packages (Hobbs and Ord, 2015, p 236). We have used *LastWave* (Arneodo et al., 2003).
- The singularity spectrum is derived from the scalogram using suitable software. We have used *LastWave* (Arneodo et al., 2003) but other packages are available (see Hobbs and

Ord, 2015, p 236). This singularity spectrum gives the metrics: D_0, D_1, D_2, D_∞ and $D_{-\infty}$ (Figure 9.10 c).

- Profiles are prepared across the scalogram (Figure 9.10 b) as shown by the yellow lines. These can be at any convenient spacing. The profiles are shown in Figure 9.10 (d).
- The Hurst exponent, *H*, is calculated for each profile using $\frac{R(d)}{\sigma(d)} = \left(\frac{d}{2}\right)^H$ which is discussed in Section 6.3.1. This can be done for the initial data set and for each of the profiles in Figure 9.10 (d). The calculations can be readily done in Excel. The final results are plotted in Figure 9.10 (e). In all scalograms and Hurst analyses the wavelet scale is given as octaves (see Appendix to this chapter).

In the results shown here the scalogram has been prepared using *Mathematica*; the singularity spectrum has been prepared using *LastWave*. The Hurst exponents have been calculated from the Mathematica derived scalogram.

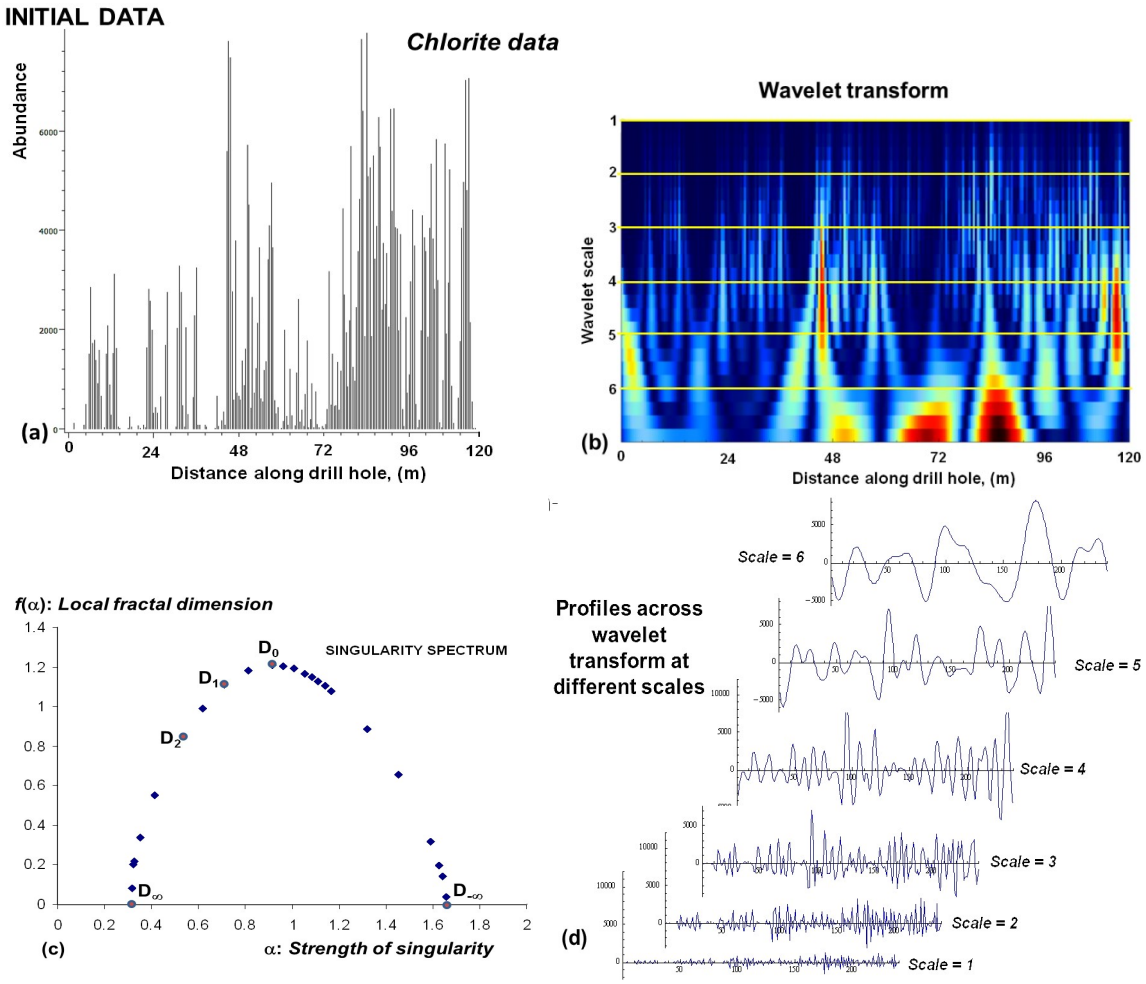

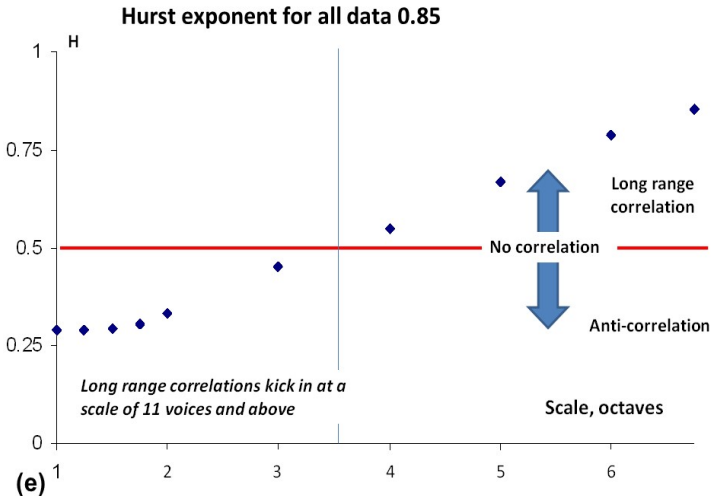

Figure 9.10. Summary of work flow in analysing data. (a) The raw data. Chlorite hyperspectral data collected at 0.5 m intervals along a diamond drill core. (b) Wavelet transform scalogram of the data. Yellow lines indicate the section profiles shown in (d). (c) Singularity spectrum with important indices, D_0, D_1, D_2, D_∞, and $D_{-\infty}$, labelled. (d) Sections at different scales across the scalogram in (b). (e) Hurst exponents for each section line in (b). Hurst exponent for the raw data is 0.85. Long range correlations begin at 11 voices, marked by the vertical blue line, which corresponds to ≈ 0.9 m. At less than 8 voices the wavelet scale is smaller than the sampling interval.

9.4. Some examples.

As we have indicated, it is now routine to collect hyperspectral reflectance data for a large range of minerals such as chlorite, sericite and carbonates, including detailed changes in chemical composition, in drill holes through hydrothermal systems. Also collected are multi-element chemical analyses and assays for gold. All this data is available in digital format and so is readily available for analysis using wavelet transforms. In what follows we give some examples of analyses from gold ore bodies in the Archean Yilgarn terrain of Western Australia. We select two deposits, namely the Sunrise Dam deposit (Hill et al., 2014) which is a large deposit comprised of a number of smaller rich deposits and Imperial (Munro et al., 2016) which is a small deposit with a small gold endowment. The example from Sunrise Dam is from the GQNorth part of the ore system (Hill et al., 2014). The aim is to provide examples of the results of processing these data sets. Detailed results will be presented in a Chapters 10 and 11. Even so, with the limited examples presented here, important distinctions between the richly and poorly endowed deposits become clear.

In Figures 11, 12 and 13 we present results for the GQNorth ore body within the Sunrise deposit in the Yilgarn of Western Australia (Hill et al., 2014). The Sunrise deposit is a high nugget deposit, currently owned by AngloGold Ashanti Australia and, at 30 June 2010, had resources of 23.3 million tonnes at 2.9 grams per tonne Au for 2.17 million ounces of gold. The raw data for chlorite, sericite and gold for a drill hole 120 m long are presented in Figure (a) of each of these figures whilst the scalogram is presented in (b), the singularity spectrum in (c) and the Hurst exponent at a number of scales in (d).

Figures 14, 15 and 16 present similar data sets for chlorite, undifferentiated mica and gold, along a drill hole in the Imperial gold deposit (Munro et al., 2016) south of Kalgoorlie. In this example the drill hole is 100 m long. The Imperial deposit is presently owned by

Silver Lake Resources and is small compared to Sunrise Dam with a resource quoted at 83,700 ounces of gold.

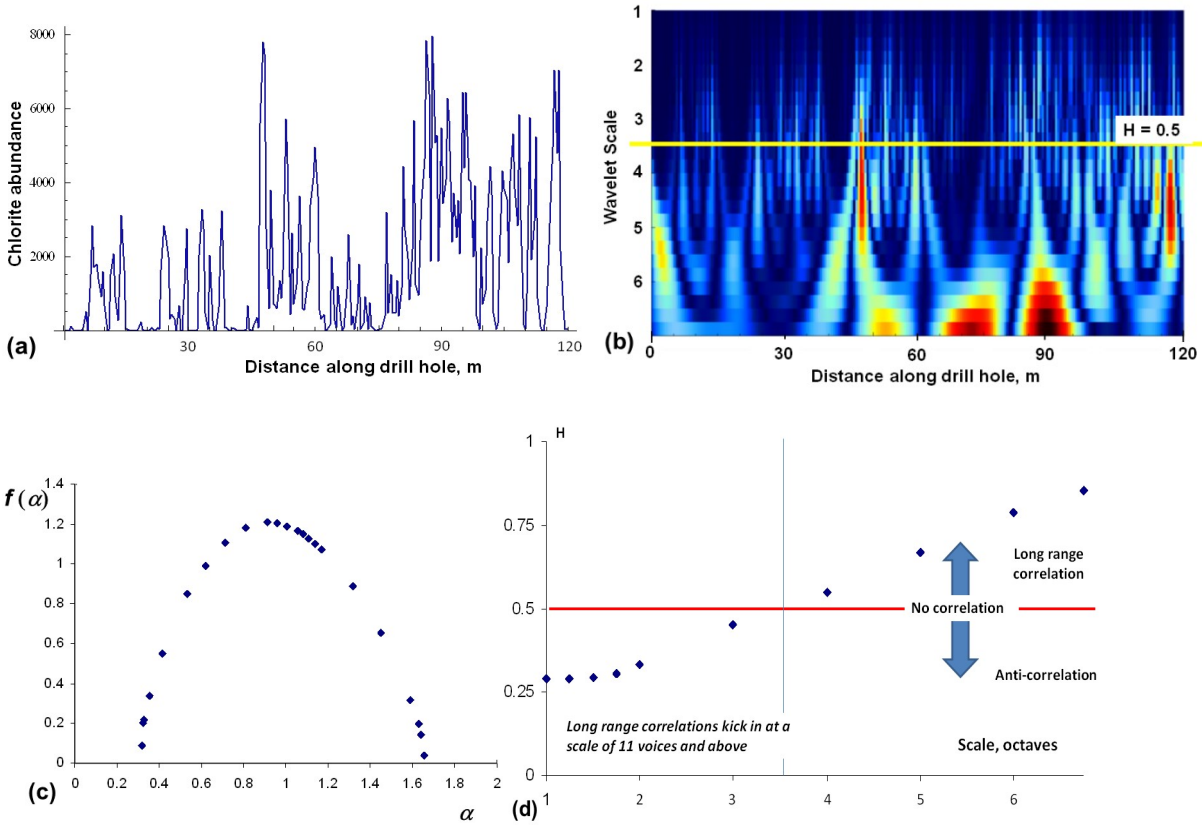

Figure 9.11. Scalograms and Hurst exponents for chlorite data, Sunrise Dam (GQNorth), Western Australia. Drill hole length 120m, sampled at 0.5 m intervals. (a) Near infra-red reflectance data. (b) Scalogram. The yellow line indicates where the Hurst exponent changes from <0.5 to >0.5. (c) Singularity spectrum. $\left(D_{-\infty} - D_{+\infty}\right) \approx 1.35$ (d) Hurst exponents at various scales showing where the Hurst exponent changes from <0.5 to >0.5. The cross-over scale is quoted as a voice (see Appendix A). In this case 11 voices corresponds to ≈ 0.9 m.

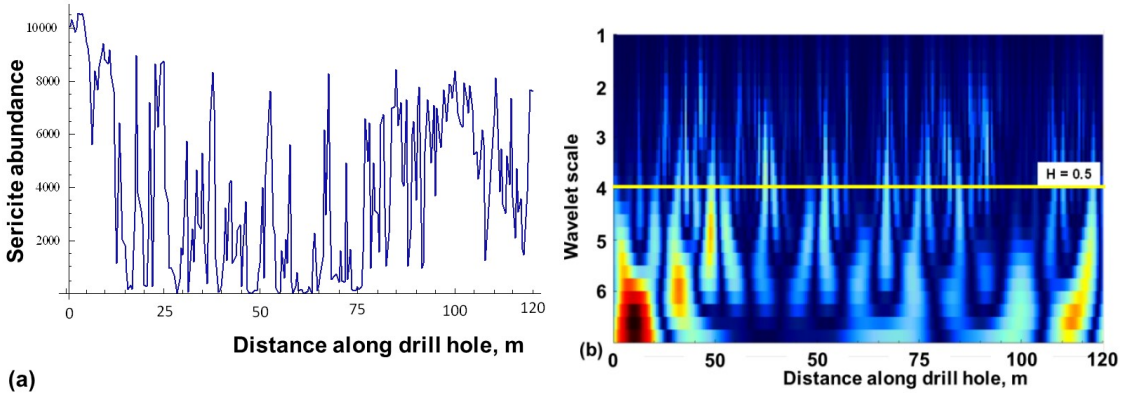

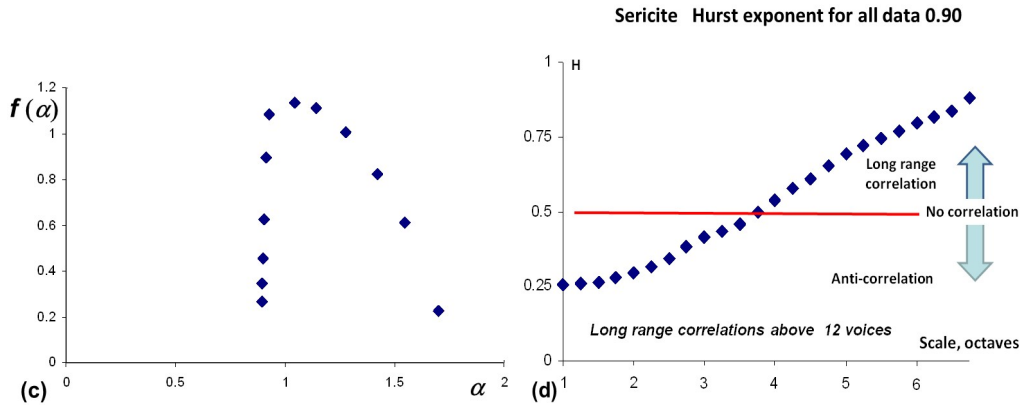

Figure 9.12. Scalograms and Hurst exponents for sericite data, Sunrise Dam (GQNorth), Western Australia. (a) Near infra red reflectance data. Data collected at 0.5 m intervals. (b) Scalogram. The yellow line indicates where the Hurst exponent changes from <0.5 to >0.5. (c) Singularity spectrum. $\left(D_{-\infty} - D_{+\infty}\right) \approx 1$ (d) Hurst exponents at various scales showing where the Hurst exponent changes from <0.5 to >0.5. The cross-over scale is quoted as a voice (see Appendix A). In this case 12 voices corresponds to ≈ 1 m.

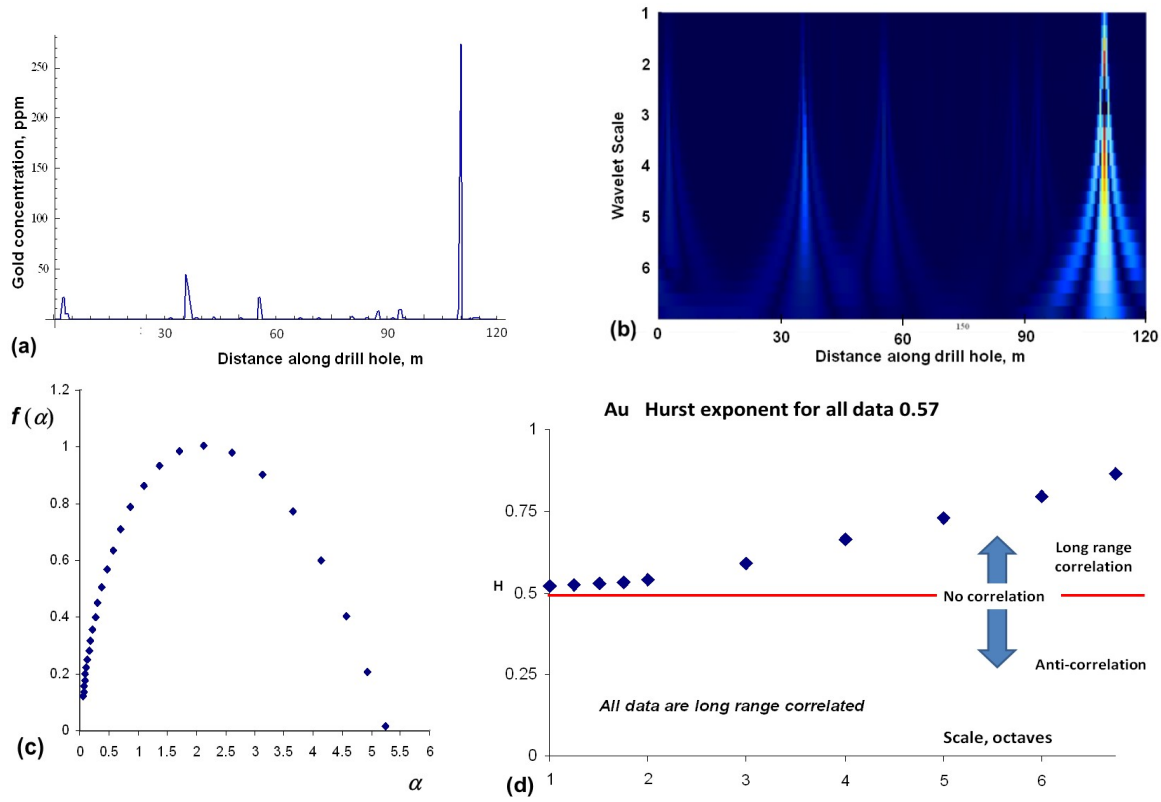

Figure 9.13. Scalograms and Hurst exponents for gold data, Sunrise Dam (GQNorth), Western Australia. Drill hole length 120m, sampled at 0.5 m intervals. (a) Assay data. (b) Scalogram. The yellow line indicates where the Hurst exponent changes from <0.5 to >0.5.(c) Singularity spectrum. $\left(D_{-\infty} - D_{+\infty}\right) \approx 5.25$. (d) Hurst exponents at various scales showing where the Hurst exponent changes from <0.5 to >0.5.

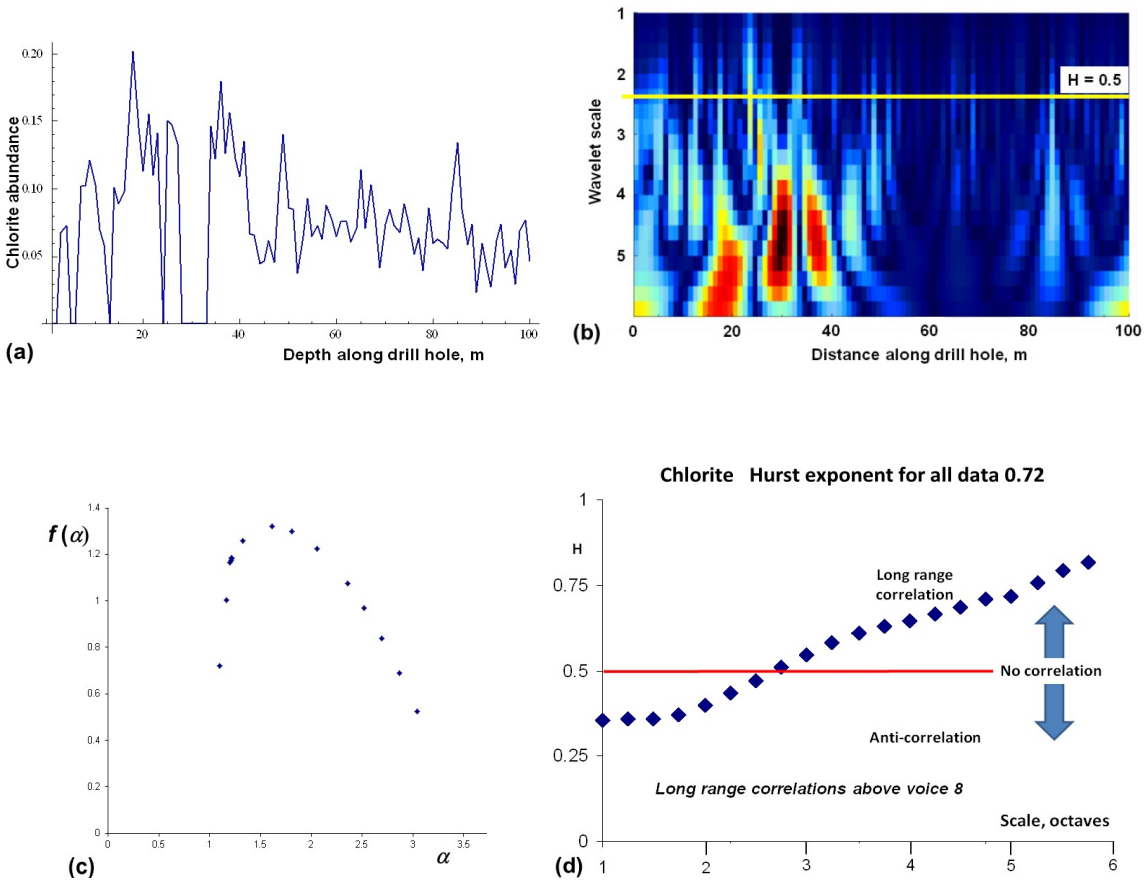

Figure 9.14. Multifractal geometry of chlorite abundance from Imperial mine, Yilgarn, Western Australia. Drill hole length 100m, sampled at 1 m intervals. (a) Abundance hyperspectral data. (b) Scalogram for data in (a). (c) Singularity spectrum for data in (a). $\left(D_{-\infty} - D_{+\infty}\right) \approx 2.5$ (d) Hurst exponents for scalogram in (b). The cross over scale of 8 voices from uncorrelated to correlated corresponds to ≈ 1 m.

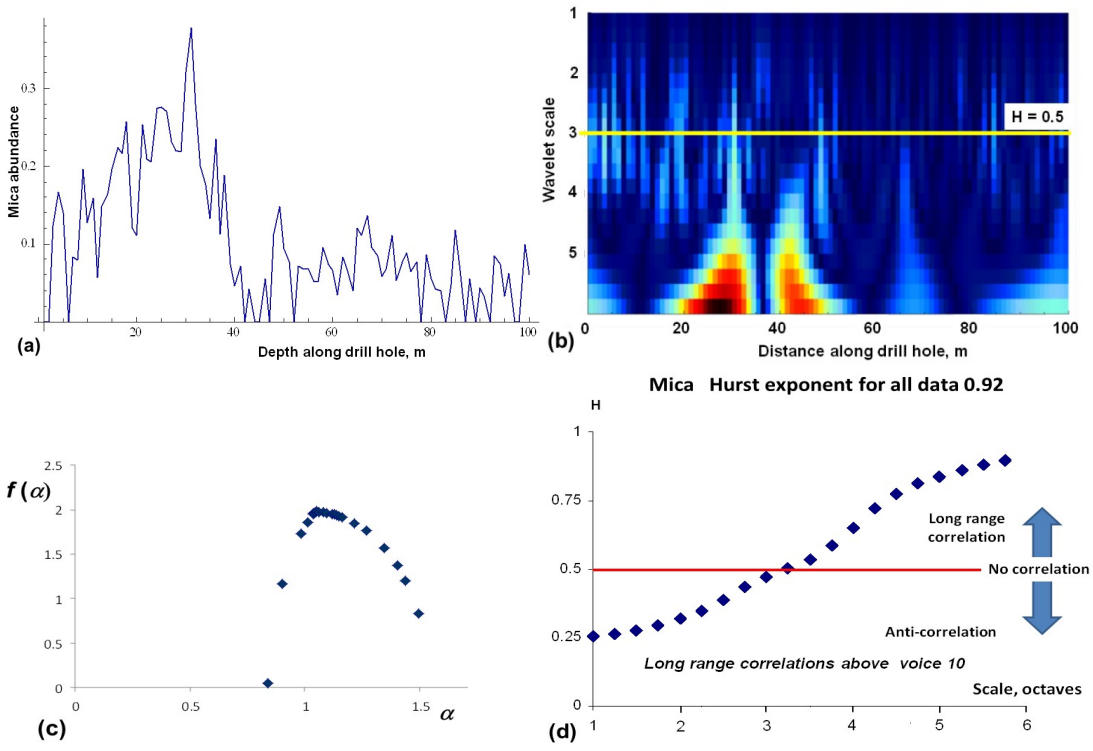

Figure 9.15. Multifractal geometry of mica abundance from Imperial mine, Yilgarn, Western Australia. Drill hole length 100m, sampled at 1 m intervals. (a) Abundance hyperspectral data. (b) Scalogram for data in (a). (c) Singularity spectrum for data in (a). $\left(D_{-\infty} - D_{+\infty}\right) \approx 0.9$ (d) Hurst exponents for scalogram in (b). The coss-0over scale of 10 voices corresponds to ≈ 1.4 m.

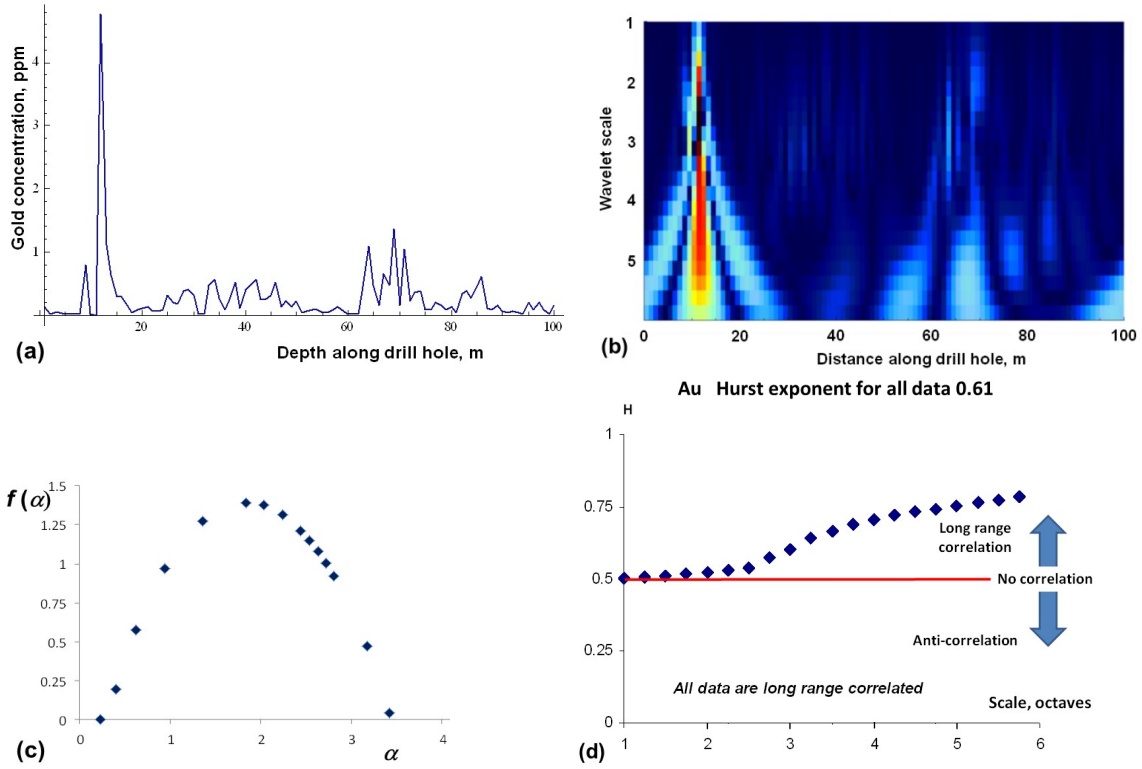

Figure 9.16. Multifractal geometry of gold concentration from Imperial mine, Yilgarn, Western Australia. Drill hole length 100m, sampled at 1 m intervals. (a) Assay data each 1 m along hole. (b) Scalogram for data in (a). (c) Singularity spectrum for data in (a). $\left(D_{-\infty} - D_{+\infty}\right) \approx 3.1$ (d) Hurst exponents for scalogram in (b).

The Yilgarn mineralised systems illustrated in this chapter show the following two characteristics:

(i) All data sets, whether they be for gold, chlorite, sericite (or mica) or breccia show well developed singularity spectra that differ quite strongly from those obtained for monofractal signals and white noise (Ihlen, 2012). This shows that although the signals appear to be stochastic they have an underlying deterministic origin. This is encouraging because it carries the promise that with further analysis (Arneodo et al., 1995) we can learn more about the underlying physical and chemical processes involved in the formation of these systems. Ideally we would like to establish the attractor for these systems since that would give clues regarding the details of the underlying mathematical framework. The construction of an attractor however requires more data than we have been able to assemble so far. The various spectra show a range of values for the metrics, D_0, D_1 and D_2 (Figure 9.10 c) which we will not explore any further here. Instead we concentrate on the values of $\left(D_{-\infty} - D_{+\infty}\right)$.

(ii) The values of $\left(D_{-\infty} - D_{+\infty}\right)$ for various spectra are summarised in Figure 9.17 (a). They clearly fall into two groups; the well endowed deposit (Sunrise Dam) shows a

very large value of $(D_{-\infty} - D_{+\infty})$ for gold relative to the less endowed deposit (Imperial). The chlorite and sericite values of $(D_{-\infty} - D_{+\infty})$ are close together for Sunrise Dam and well separated for Imperial. Of course the data set is very small and we report on larger data sets in Chapters 10 and 11 and in Munro et al. (2016). As an indication of results from larger data sets we show in Figure 9.17 (b) results from Cosmo East (a part of Sunrise Dam) and Salt Creek (with a resource of 109,390 ounces of gold) Again the high resource deposit (Cosmo East) shows a large proportion of values for $(D_{-\infty} - D_{+\infty})$ in the range 4 to 8 whereas the smaller resouce deposit (Salt Creek) has a peak at $(D_{-\infty} - D_{+\infty}) \approx 2$. Cosmo East also has this peak suggesting that the deposit has some less endowed parts. Both deposits have similar values of $(D_{-\infty} - D_{+\infty})$ for chlorite.

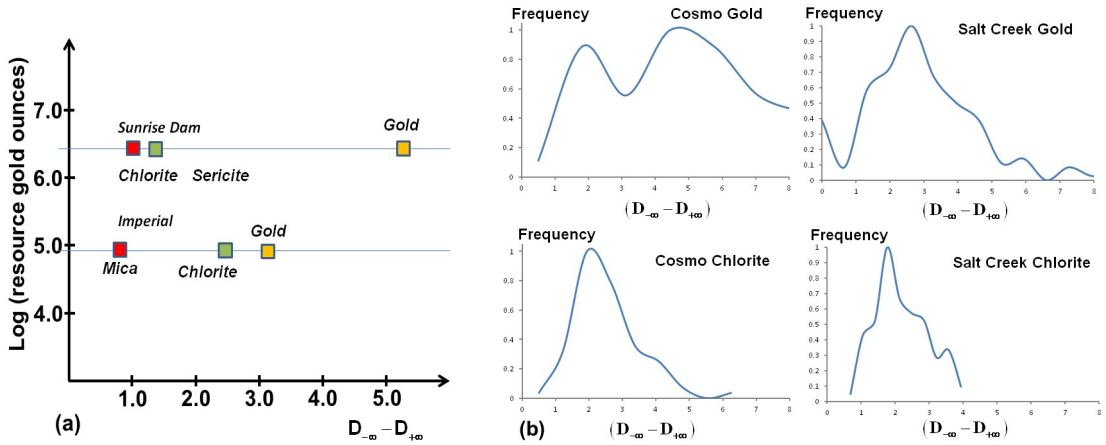

Figure 9.17. Synthesis of $(D_{-\infty} - D_{+\infty})$ data. (a) $(D_{-\infty} - D_{+\infty})$ data from GQNorth and Imperial ore bodies, Sunrise Dam. (b) Normalised frequency $(D_{-\infty} - D_{+\infty})$ data from Cosmo East (Sunrise Dam) and Salt Creek ore bodies. Numbers of samples: 40 gold, Cosmo East. 79 chlorite, Cosmo East. 170 gold, Salt Creek. 93 chlorite, Salt Creek.

9.8. The relation to dynamical systems.

In Figure 9.18 we show a model proposed by Zapperi et al. (1995) and discussed by Ihlen and Vereijken (2010). The model is a cellular automata that activates adjacent nodes according to a probability, p. If $p < 0.5$ the model evolves to a sub-critical state with relatively small values of $(D_{-\infty} - D_{+\infty})$. At $p = 0.5$, which corresponds to a critical state, $(D_{-\infty} - D_{+\infty})$ suddenly increases and attains relatively high values for $p > 0.5$, corresponding to supercritical states. This model is a form of self-organised criticality. Very similar results are obtained by Ihlen and Vereijken (2010) for a multiplicative cascade process due to Chainais (2006); this model does not propose self-organised criticality as an inherent process. If one adopts the Ihlen-Vereijken model, the data reported here suggest that well endowed ore

bodies are super-critical whereas less endowed ore bodies are sub-critical and this is reflected in $\left(D_{-\infty} - D_{+\infty}\right)$ values.

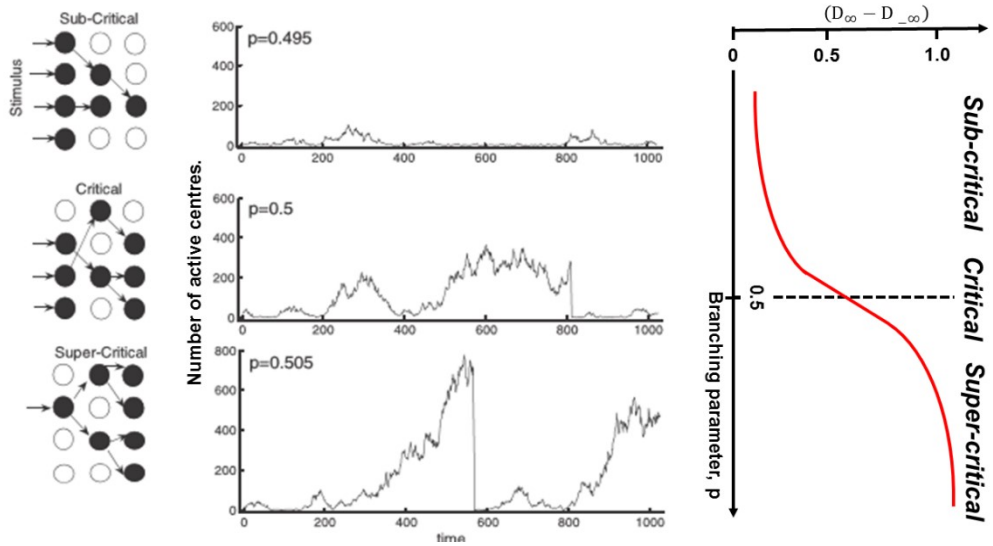

Figure 9.18. Results of self-organized branching process (after Ihlen and Vereijken, 2010). Left column portrays the model whereby an initial array of centres (black: active and white: inactive) gives rise to other centres with a probability of formation, p. If $p < 0.5$ the likelihood is that inactive centres will be produced and the process ultimately stops. The resultant signal is given in the top central panel. If $p = 0.5$ the behaviour is given in the centre panel (middle). If $p > 0.5$ strongly intermittent behaviour results as in the centre panel, bottom. The behaviour of the quantity $\left(D_{-\infty} - D_{+\infty}\right)$ as p varies from 0 to 1 is given in the right panel. $\left(D_{-\infty} - D_{+\infty}\right)$ varies from small values for $p < 0.5$ to larger values for $p > 0.5$.

9.9. Relation to spatial statistics.

Classical spatial statistics applied to the generation of ore body grade and block models assumes that it is possible to define a mean (or expected value) for the grade distribution and that there are no long range correlations in the distribution of mineralisation. Both these assumptions have been shown in this chapter to be unwarranted. Rationalisation of this observation with classical statistical approaches is yet to be achieved. For the moment we observe that four different categories of mineralisation can be distinguished on the basis if the singularity width, $\left(D_{-\infty} - D_{+\infty}\right)$, and the spatial scale at which long range correlations become important; we call this scale $L^{correlation}$. If $\left(D_{-\infty} - D_{+\infty}\right)$ is small ten it is obsereved that the ore body is not well endowed and *vice versa*. If $L^{correlation}$ is on the scale of mining operations then prediction of grade is relativley easy and the ore body can be mined with reasonable confidence. If $L^{correlation}$ is large compared to the mining operations then prediction seems to be difficult and the ore body is not easy to mine. These distinctions are shown in Figure 9.19.

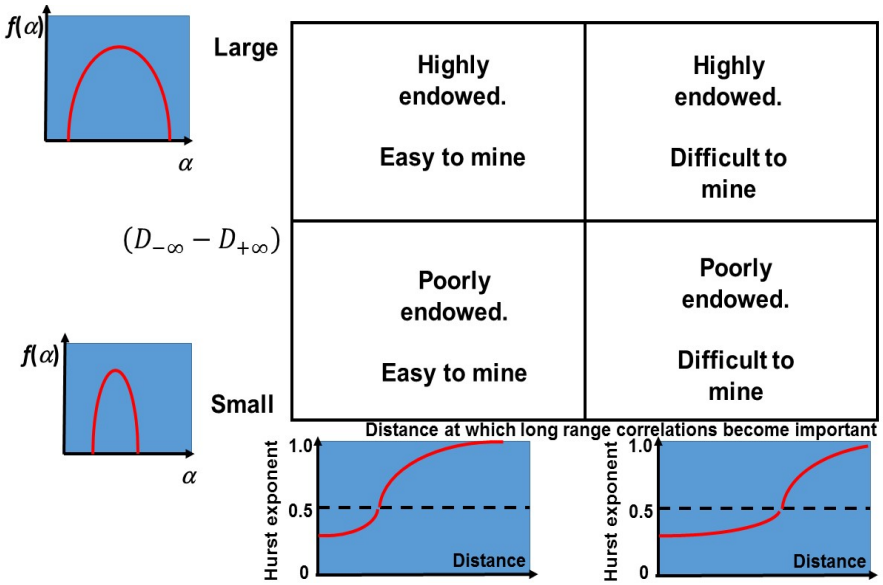

Figure 9.19. A classification of ore bodies on the basis of width of the singularity spectrum and whether long range correlations appear at small or large spatial scales relative to the scale of day to day mining operations.

9.10. Summary.

In viewing hydrothermal mineralising systems as open flow chemical reactors it becomes clear that these systems, in order to continue operating, undergo a number of phase changes. The dominant transitions are unaltered $\rightarrow$ altered, which is an exothermic transition, un-mineralised $\rightarrow$ mineralised, which is an endothermic transition, and undeformed $\rightarrow$ veined/brecciated, which is a combination of exothermic (fracturing, breakage, precipitation of carbonates and quartz) and endothermic (precipitation of sulphides and non-hydrous silicates such as albite) processes. The competition between these processes means that the reactor behaves in a non-linear, chaotic manner with chaotic spatial distributions of alteration, mineralisation and veining/brecciation.

Although chaotic, all of these spatial distributions are deterministic in origin even though they appear as apparently stochastic patterns. Such patterns are multifractal and the deterministic origin is revealed in singularity spectra that are significantly broader than spectra arising from white noise. The width, $\left(D_{-\infty} - D_{+\infty}\right)$, of these spectra appear to be related to the mineralised endowment of the system so that weakly endowed systems have narrow spectra whereas strongly endowed systems have wide spectra. This can be interpreted as a transition from sub-critical to super-critical behaviour if one adopts a self-organised critical model or as a transition from weak to strong long range interactions if one adopts a multiple-cascade model.

All systems show long range spatial correlations if one uses the raw data but if one measures the spatial correlations at individual length scales, these systems show short range anti-correlations and long range positive correlations. We propose that the short range anti-correlations correspond to relatively small fluid mixing cells of the order of 10 m across that are responsible for the intensity of mineralisation and alteration. The long range spatial correlations indicate that the system has established a correlated fluid flow system on the scale of the sampling length. It is notable that at small spatial scales gold distribution has

Hurst exponent close to 0.5 which means that at that scale gold distributions are uncorrelated. Any correlations arise at relatively spatial large scales. A distinction between ore bodies that are easy to mine and those that are difficult to mine can be made on the basis of the scale where long range correlations become important compared to the spatial scale of day to day mining operations.

Appendix. Octaves and voices in scalograms.

In Mathematica© a scaling parameter, s, of the wavelet signal is defined in terms of an equal tempered scale given in powers of 2 and divided into octaves and subdivided into 4 "voices". Thus the scaling parameter is divided into the array expressed in (A.1).

[1,1], [1,2], [1,3], [1,4] *octave* 1, *voices* 1 to 4

[2,1], [2,2], [2,3], [2,4] *octave* 2, *voices* 5 to 8

……

[n_{oct},1], [n_{oct},2], [n_{oct},3], [n_{oct},4] *octave* n_{oct}, *voices* ($4n_{oct}$ -3) to $4n_{oct}$ (A.1)

n_{oct} is the total number of octaves representing the wavelet signal and is given by

$$n_{oct} = \left\lfloor \log_2\left(\frac{n}{2}\right) \right\rfloor$$

where n is the number of data points in the signal (equally spaced) and $\lfloor x \rfloor$ is the floor to x, that is, the largest integer smaller than x. Thus for n = 240, n_{oct} = 6. If n is the number of data points for gold or chlorite along a drill hole n metres long then n is expressed in metres.

The smallest wavelet scale, α_{scale}, for the Mexican hat mother wavelet is given by

$$\alpha_{scale} = \left[\left(2\pi\sqrt{\frac{2}{5}}\right)\sigma\right]^{-1}$$

where σ is the width of the hat, taken to be equal to one so that α_{scale} = 0.25165 units. The units correspond to those used to measure the distance between points. The scaling parameter for a particular octave and voice is given by

$$s_{octave,voice} = \alpha_{scale} 2^{octave-1} 2^{voice/n_{voice}}$$

where, in Mathematica© , n_{voice} is taken to be 4 so that

$$s_{1,1} = 0.25165 \times 2^{1-1} 2^{1/4} = 0.299359$$

and each successive voice differs from the one smaller by a factor of $2^{1/4}$ or 1.19.

Thus, if the signal consists of 240 points each 1m apart, n_{oct} = 6 and the array (A.1) becomes

[0.299359], [0.355881], [0.423217], [0.503292] *octave* 1, *voices* 1 to 4

[0.598519], [0.711763], [0.846433], [1.00658] *octave* 2, *voices* 5 to 8

[1.19704], [1.42353], [1.69287], [2.01317]	*octave* 3, *voices* 9 to 12	
[2.39407], [2.84705], [3.38574], [4.02634]	*octave* 4, *voices* 13 to 16	
[4.78815], [5.6941], [6.77146], [8.05267]	*octave* 5, *voices* 17 to 20	
[9.5763], [11.3882], [13.5429], [16.1053]	*octave* 6, *voices* 21 to 24	(A.2)

In this case, the voices, in square brackets, are expressed in metres.

The vertical axis on the scalogram can be represented by the array (A.1) or as (A.2) or more simply by just the octaves, numbered 1 to n_{oct}. We use only the octaves but to convert scales to metres, as in the Hurst exponent measurements, the above discussion is relevant.

Recommended reading.

Arneodo